UC Berkeley

UC Berkeley Previously Published Works

Title

Non-volatile electric-field control of inversion symmetry

Permalink

https://escholarship.org/uc/item/2zf302bc

Journal

Nature Materials, 22(2)

ISSN

1476-1122

Authors

Caretta, Lucas

Shao, Yu-Tsun

Yu, Jia

et al.

Publication Date

2023-02-01

DOI

10.1038/s41563-022-01412-0

Copyright Information

This work is made available under the terms of a Creative Commons Attribution License, available at https://creativecommons.org/licenses/by/4.0/

Peer reviewed

eScholarship.org Powered by the California Digital Library
University of California

Nonvolatile Electric-Field Control of Inversion Symmetry

Lucas Caretta[1,14,*], Yu-Tsun Shao[2,14], Jia Yu[3], Antonio B. Mei[4], Bastien F. Grosso[5], Cheng Dai[6], Piush Behera[1], Daehun Lee[3], Margaret McCarter[7], Eric Parsonnet[7], Harikrishnan K.P.[2], Fei Xue[6], Xiangwei Guo[8,9], Ed Barnard[10], Steffen Ganschow[11], Zijian Hong[8], Archana Raja[10], Lane W. Martin[1,12], Long-Qing Chen[6], Manfred Fiebig[5], Keji Lai[3], Nicola A. Spaldin[5], David A. Muller[2,13], Darrell G. Schlom[4,11,13], Ramamoorthy Ramesh[1,7,12,*]

[1]*Department of Materials Science and Engineering, University of California, Berkeley, California, USA*
[2]*School of Applied and Engineering Physics, Cornell University, Ithaca, New York, USA.*
[3]*Department of Physics, University of Texas, Austin, Texas, USA*
[4]*Department of Materials Science and Engineering, Cornell University, Ithaca, New York, USA.*
[5]*Department of Materials, ETH Zurich, Zurich, Switzerland.*
[6]*Department of Materials Science and Engineering, The Pennsylvania State University, University Park, Pennsylvania, USA*
[7]*Department of Physics, University of California, Berkeley, California, USA*
[8]*State Key Laboratory of Silicon Materials, School of Materials Science and Engineering, Zhejiang University, Hangzhou, Zhejiang, China*
[9]*Hangzhou Global Scientific and Technological Innovation Center, Zhejiang University, Hangzhou, Zhejiang, China*
[10]*Molecular Foundry, Lawrence Berkeley National Laboratory, Berkeley, California, USA*
[11]*Leibniz-Institut für Kristallzüchtung, Max-Born-Str. 2, Berlin, Germany*
[12]*Materials Sciences Division, Lawrence Berkeley National Laboratory, Berkeley, California, USA*
[13]*Kavli Institute at Cornell for Nanoscale Science, Ithaca, New York, USA*
[14]*These authors contributed equally.*

*Correspondence to: rramesh@berkeley.edu, caretta@berkeley.edu

Abstract

In condensed-matter systems, competition between ground states at phase boundaries can lead to significant changes in material properties under external stimuli[1–4], particularly when these ground states have different crystal symmetries. A key scientific and technological challenge is to stabilize and control coexistence of symmetry-distinct phases with external stimuli. Using $BiFeO_3$ (BFO) layers confined between layers of the dielectric $TbScO_3$ (TSO) as a model system, we stabilize the mixed-phase coexistence of centrosymmetric and non-centrosymmetric BFO phases at room temperature with antipolar, insulating and polar, semiconducting behavior, respectively. Application of orthogonal in-plane electric (polar) fields results in the reversible, nonvolatile interconversion between the two phases, hence removing and introducing centrosymmetry in the system. Counterintuitively, we find that an electric field can 'erase' polarization in the system,

resulting from the anisotropy in octahedral tilts introduced by the interweaving TSO layers. Consequently, this interconversion between centrosymmetric and non-centrosymmetric phases coincides with simultaneous changes in the non-linear optical response of over three orders of magnitude, a change in resistivity of over five orders of magnitude, and control of the microscopic polar order. Our work establishes a materials platform allowing for novel cross-functional devices which take advantage of changes in optical, electrical, and ferroic responses, and also demonstrates octahedral tilts as an important order parameter in materials interface design.

Introduction

Crystal symmetry in condensed-matter materials largely dictates their micro- and macro-scopic properties[5], and in turn, their functionalities. Much effort has been devoted to designing and tuning symmetry in solid-state materials[6–12], with ferroelectrics being a particularly pervasive example of broken inversion symmetry[13] (Extended Data Fig. 1a,b). For example, inversion symmetry in antiferroelectric materials can be broken by a strong electric field, converting the system into a volatile, field-stabilized polar phase[13]. Stabilization of competing low-energy ground states – *e.g.*, polar and antipolar phases – offer the potential to interconvert between states with different crystallographic symmetries and order parameter-energy landscapes. Such competing phases are often realized by growth of ferroelectric superlattices using layer-by-layer deposition techniques and the utilization of *ab initio* calculations. These competing phases include nontrivial polar textures[14–18], room-temperature magnetoelectric materials[19], improper ferroelectrics[20–24], and antipolar phases[25,26] that have resulted from the interplay among strain, electrostatic, and gradient energies. There have been efforts to manipulate between these distinct phases with external stimuli, such as electric fields[27,28], resonant optical excitations[11,12,29], and strain[30,31]; however, these conversions are often between two non-centrosymmetric states, volatile in nature, or irreversible. The ability to both *remove* and *introduce* symmetry (and in particular, polarization) with an electric field in a nonvolatile fashion remains elusive, as electric fields generally only break symmetries.

Here, we show that this nonvolatile interconversion is indeed possible using confined $BiFeO_3$ (BFO) layers as our model system. We stabilized mixed-phase coexistence of a non-centrosymmetric polar and a centrosymmetric antipolar phases by utilizing: (i) a discontinuity of the local polarization at the heterointerface; (ii) a lattice mismatch arising from the different lattice parameters of the two layers; and (iii) a discontinuity in the sense and direction of the octahedral rotations in the two layers, which we achieve by using $TbScO_3$ (TSO) as our epitaxial dielectric interleaving layers. The polar and antipolar phases are identified and characterized using a combination of high-resolution and four-dimensional (4D) scanning transmission electron microscopy (STEM), piezoresponse force microscopy (PFM), microwave impedance microscopy (MIM), confocal second harmonic generation (SHG), transport measurements, and density-functional theory (DFT). Moreover, using applied electric fields, we interconvert between the polar non-centrosymmetric and antipolar centrosymmetric phases reversibly and in a nonvolatile fashion. With this electric field-driven phase transformation, we show that the applied electric field not only removes centrosymmetry to stabilize polar order, but the electric (*i.e.,* polar) field can remarkably re-introduce centrosymmetry and stabilize antipolar order, effectively "erasing" the polarization in the material. We further demonstrate that electric-field manipulation of the crystal symmetry also manifests as concomitant non-volatile, dramatic changes in both the second harmonic generated (SHG) signal and the DC and microwave conductivity. Such large changes in functional materials properties as a result of an electric field-induced symmetry phase transformation open pathways to new opto-electronic devices and highlight a new design scheme and materials platform for developing phase-change-based memory and logic.

Mixed-Phase Coexistence of Non-centrosymmetric and Centrosymmetric Phases

Recent studies have shown that various low-energy phases and polytypes of BFO can be stabilized using different experimentally-achievable boundary conditions[23,25,26,32–35]. The calculated energies and structures of such phases as a function of their respective unit cell sizes (Methods, Extended data Fig. S21) are shown in Fig. 1a. Of note is the presence of phases with different crystal symmetries in

energetic proximity to the *R*3*c* ground state, including a centrosymmetric *Pnma* phase, as well as large unit cell, non-centrosymmetric *Pc* phases with polarization waves in which the relative stability is a function of the wavelength.

The energetic proximity of these BFO phases with different symmetry suggests the possibility of stabilizing multiple coexisting phases with significantly different properties. To investigate this possibility, epitaxial superlattices of $[(BFO)_n/(TSO)_m]_{20}$ for n = 11 – 20, m = 10 unit cells were synthesized by reactive molecular beam epitaxy (MBE) on $GdScO_3$ and TSO $[110]_O$ substrates (the O denotes orthorhombic orientation; Methods). High-angle annular dark field (HAADF) STEM imaging of a $[(BFO)_{14}/(TSO)_{10}]_{20}$//GSO superlattice shows atomically sharp interfaces, with no obvious presence of crystallographic defects (Fig. 1b, Extended Data Fig. 2, and the X-ray reciprocal space maps in Extended Data Fig. 3). To study the symmetry of the BFO layers, we employed scanning convergent beam electron diffraction (SCBED) coupled with an electron microscopy pixel array detector (EMPAD)[36,37] (Methods). The bright-field (BF) image reconstructed from the SCBED dataset (Fig. 1c) reveals the coexistence of two distinct phases within the BFO layers exhibiting bright and dark contrast, respectively. A symmetry analysis (Extended Data Fig. 4) identifies the two phases as the non-centrosymmetric *Pc* phase (dark regions, Fig. 1c) and a centrosymmetric *Pnma* phase (bright regions, Fig. 1c).

In polar crystals, the charge redistribution associated with ferroelectric polarization leads to intensity asymmetry in polarity-sensitive Friedel pairs of Bragg reflections in the CBED pattern; hence, SCBED in combination with dynamical diffraction simulations enables polarization mapping at sub-nanometer resolution[38–40] (Supplementary Text 1). The arrows map the polarization from the non-centrosymmetric *Pc* BFO phase (Fig. 1d corresponding to the dark regions, Fig. 1c), which shows continuously winding electric dipoles resembling a polarization wave or a series of half vortices. The continuous rotation of the polarization can be represented by $\nabla \times P$(denoted by the blue/red color overlay, Fig. 1d). In addition to the rotating polarization within the wave, there is a net in-plane

polarization along the wave direction ($[100]_{pc}$ or $[\bar{1}00]_{pc}$) that can vary in antiparallel direction between and within each BFO layer in the superlattice. The atomic structure of the coexisting centrosymmetric *Pnma* phase was also probed (Fig. 1e and f, corresponding to the bright regions, Fig. 1c) by HAADF-STEM images along two projections of the crystallographic zone axes (*i.e.*, $[100]_{pc}$ and $[010]_{pc}$, where pc denotes pseudocubic indices). Overlaid on these atomic images are the polar-vector maps of the bismuth-ion displacement, which shows the antipolar "up-up-down-down" order along the $[011]_{pc}$ projection also observed elsewhere[25,26,34]. The polar and antipolar nature of the two phases is confirmed with charge-voltage hysteresis loops (Extended Data Fig. 5 and see also Supplementary Text 2. Therefore, we have stabilized two low-energy phases of BFO with non-centrosymmetric polar and centrosymmetric antipolar properties, where the net polarization of the polarization wave ($[100]_{pc}$ or $[\bar{1}00]_{pc}$) phase orients orthogonally to the local dipoles in the antipolar phase ($\langle 011 \rangle_{pc}$). Interestingly, the saturated polarization of both phases, as shown in Extended Data Fig. 5, are similar, suggesting that the high field state of the antipolar phase is the zero field phase of the polar phase. HAADF-STEM taken along the $[100]_{pc}$ zone axis reveals the atomically sharp boundary between the coexisting BFO phases (Fig. 1g and Extended Data Fig. 6), suggestive of a first-order phase transformation[41].

Such mixtures of nearly energetically degenerate phases have been the framework used to elicit significant responses to external stimuli[1–4,42]. We now demonstrate such large, simultaneous changes in piezoelectricity, optical SHG, microwave response, and DC conductivity in the mixed-phase superlattices. Lateral PFM phase imaging (Fig. 2a), in which the contrast is sensitive to in-plane polarization along the $[100]_{pc}$ of the uppermost BFO layer in the sample reveals distinct, stripe-like regions of high piezoelectric response (white and dark brown regions) and zero piezoelectric response (orange regions) on the order of several micrometers in width and extending for hundreds micrometers along the $[010]_{pc}$. Consistent with the HR-STEM vector mapping, the high piezoresponse regions are comprised of the polar phase of BFO, where white subdomains have net polarization along the $[\bar{1}00]_{pc}$ and dark-brown subdomains have net

polarization along the antiparallel $[100]_{pc}$ (Fig. 2a). Regions of zero piezoresponse (orange regions, Fig. 2a) correspond to the antipolar BFO phase. These observations are confirmed with additional lateral and out-of-plane PFM measurements (Extended Data Fig. 7). We note that the relative stability of each phase can be controlled by tuning the thickness of the BFO layers in the superlattice. As shown by lateral PFM images (Extended Data Fig. 8 and 9) and confirmed with phase field simulations (Extended Data Fig. S23), small unit cell changes in the BFO thickness from 11 to 19 unit cells transform the superlattice from a uniform antipolar state to a uniform polar state, while changing the strain state via substrate selection changes the length scales of the domains (Supplementary Text 3).

Nonlinear Optical Response of Mixed-Phase Coexistence

The coexistence of polar and non-polar symmetries also results in a dramatic spatial variation of the non-linear optical response of the material. A SHG map (Methods) of a nearby region on the same sample (Fig. 2b) provides, unlike PFM, information that is integrated throughout the thickness of the film[43]. Furthermore, the comparison of PFM and SHG signals helps to distinguish true polarization effects from band-structural changes of the piezoelectric or nonlinear optical susceptibilities that may occur because of the phase transition. We select a normal-incidence optical geometry, for which the transversally polarized fundamental and, thus, SHG light probes the in-plane symmetry breaking. Distinct centrosymmetric antipolar (dark intensity) and non-centrosymmetric polar (bright intensity) stripe-like phases of BFO are also seen (Fig. 2b, also see Extended Data Fig. S20). The distributions of the brightness within the polar regions differ, however, because of SHG interference occurring at the domain walls and the possibility of domains of different polarization stacked perpendicular to the film surface. Local SHG polar plots from both BFO phases, in which the incident light polarization is varied and the corresponding vertically (Fig. 2c) or horizontally (Fig. 2d) polarized emitted light at the second harmonic is analyzed, are also provided. The non-centrosymmetric polar phase (red circles, Fig. 2c,d) shows a two-lobed angle-dependent SHG intensity profile, with two additional minor lobes, consistent with the space group *Pc* (point-group symmetry *m*) (Fig. 1a) obtained from the CBED analysis (Extended Data Fig. 4

and SHG selection rules in Methods). On the other hand, the centrosymmetric antipolar phase (green squares, Fig. 2c,d) has no measurable SHG signal regardless of the polarization of the incoming light or analyzed SHG light, as expected from the *Pnma* space group (point-group *mmm*) observed in the CBED analysis (Extended Data Fig. 4). Additional PFM phase images and SHG maps are provided (Extended Data Figs. 10 and 11) which scrutinize the spatial correlation of the PFM and SHG signals on the sample. The dramatic difference in non-linear optical response from each phase is further highlighted in the line scan (Fig. 2e, dashed white arrow of Fig. 2b), where the SHG intensity is enhanced by nearly five orders of magnitude in the polar phase relative to the antipolar phase. Consistent with the similar energies of the two phases found in *ab-initio* calculations (Fig. 1a), the piezoelectric, SHG, and CBED data confirm the mixed-phase coexistence of a centrosymmetric antipolar phase and a non-centrosymmetric polar phase.

Dielectric Response and Conductivity of Mixed-Phase Coexistence

We explore the changes in dielectric permittivity accompanied by such changes in symmetry, which are often observed during phase transitions in ferroelectric systems (*e.g.*, in a temperature-driven phase transition)[7]. The spatially resolved dielectric response and AC conductivity of the superlattices was probed by scanning microwave impedance microscopy[44] (MIM; Methods). First, by performing PFM with the shielded MIM tip[45], we independently confirmed the coexistence of the mixed polar and antipolar phases in a separate $[(BFO)_{14}/(TSO)_{10}]_{20}$ superlattice grown on a TSO substrate (Fig. 3a). We note that despite the growth of this nominally identical superlattice on a different substrate (strain state), the mixed-phase coexistence is persistent, only manifesting as a difference in length scales of the domains and not any differences in the nature of the phases formed (also see Extended Data Fig. S9). The imaginary (MIM-Im; Fig. 3c) and real (MIM-Re; Fig. 3c) parts of the 2.513 GHz MIM impedance were acquired on the same area as the PFM. The one-to-one correlation between the PFM and MIM images is apparent, with the polar phase showing a significantly enhanced signal compared to the antipolar phase, regardless of the polarization direction. We estimated the dielectric contribution to the MIM-Im contrast by performing finite-element analysis (FEA)[46] of the near-field interaction for the specific tip-sample

configuration (Extended Data Fig. 12, and Supplementary Text 4). We plot the simulated MIM-Im signal as a function of the permittivity of the BFO (Extended Data Fig. 12c). Assuming a dielectric constant $\varepsilon_r \sim 60$ in the polar phase[47,48], we estimated the relative dielectric constants between the two phases by comparing FEA simulation with the magnitude of experimentally-observed MIM-Im signal (Fig. 3b), yielding $\varepsilon_r \approx 30$ for the antipolar phase. This is qualitatively consistent with independent dielectric measurements at low frequencies (Extended Data Fig. 13 and Supplementary Text 5). Next, to determine the conductivity contribution to the MIM contrast, we plot the simulated Re- and Im-MIM signals as a function of sample conductivity[46] (σ; Extended Data Fig. 12d), with the dielectric contribution to the MIM signal (Extended Data Fig. 12c) accounted for by a vertical shift in the MIM-Im curve relative to the MIM-Re curve. Importantly, the small but measurable contrast in the experimentally-observed MIM-Re channel (Fig. 3c) is indicative of a finite GHz conductivity in the non-centrosymmetric polar phase (Supplementary Text 4 and Extended Data Fig. 12). Surprisingly, the simulated σ-dependent MIM contrast (Extended Data Fig. 12) suggests that the polar phase has a conductivity of ~1 S/m (*i.e.*, a resistivity of ~100 $\Omega \cdot$cm), over the frequency range of 100 MHz to 3 GHz (Extended Data Fig. 12e,f). The width of the grey region denotes the range of σ values within experimental uncertainty. Since this resistivity is approximately 5-6 orders of magnitude lower than that of bulk BFO, the MIM results strongly suggest that the polar phase displays semiconducting behavior, whereas the antipolar phase is insulating. Similar measurements performed on a nominally identical superlattice grown on a GSO substrate is shown in Extended Data S17.

DFT calculations indicate that the band gaps of the polarization wave and antipolar phases in their hypothetical bulk forms are very close to that of the bulk ground-state *R*3*c* phase (2.15 eV, see Extended Data Fig. 14 and Methods). However, a supercell calculation with a slab of two layers of the polarization wave *Pc* phase alternating with two layers of *Pnma* $BiFeO_3$ phase frozen in their bulk structures, yields a significant 0.45 eV reduction in the band gap of the polarization wave phase to 1.7 eV (Extended Data Fig. 14c-d). The calculated layer-by-layer and wave-polarization-resolved densities of

states (Figs. 3e and f and Extended Data Fig. 14e-g) reveal that the effective band-gap reduction is the result of an alternating band bending caused by the built-in electric fields induced by the local $\pm[001]_{pc}$-oriented components of the wave polarization perpendicular to the net polarization of the phase. This large electrostatic reduction in the effective bandgap is responsible for the significant enhancement in conductivity seen in the MIM results (Supplementary Text 8). Moreover, the large bandwidth of conduction observed in MIM at MHz and GHz frequencies suggests that the conduction is mediated by electrons, and not extrinsic effects, such as oxygen vacancy migration[49]. X-ray absorption spectroscopy obtained via spatially-resolved photoemission electron microscopy on a mixed-phase superlattice also confirms the Fe^{3+} valence state (Extended Data Fig. S24). We note that contrary to previous work on one-dimensional conduction observed at ferroelectric domain walls (DWs)[50,51] and phase boundaries[52], the electron conduction observed here occurs through the bulk of the polar BFO phase and does not rely on the presence of defects (DWs and phase boundaries). Moreover, it is isotropic in nature and is a direct manifestation of the confinement of the polarization wave in a superlattice structure.

Electric Field Control of Centrosymmetry

The phase coexistence and its impact on the physical properties lays the foundation for the study of pathways to interconversion between the two phases with an applied electric field. For this purpose, test structures were fabricated by lithographically patterning a set of orthogonal in-plane electrodes that enable the application of a lateral electric field along both $[100]_{pc}$ and $[010]_{pc}$ (Methods and Extended Data Fig. 15). Using these structures, we measured the field-dependent SHG concurrently with in-plane DC transport. Starting in the virgin, mixed-phase state (Fig. 4a), upon applying a lateral electric field along the $[010]_{pc}$, we observe the conversion of the polar phase (strong SHG signal) to the antipolar phase (no SHG signal) in a nonvolatile fashion (Fig. 4b). We emphasize here that, remarkably, an application of an electric (*i.e.* polar) field along the $[010]_{pc}$ eliminates the net polarization and stabilizes the antipolar state. A similar effect is observed with the application of a negative bias along this direction (*i.e.*, along

the $[0\bar{1}0]_{pc}$; Extended Data Fig. 11 and Supplementary Text 3). Grey regions within the SHG images denote the lithographically-defined electrodes, where the electric field direction and magnitude are denoted above each SHG panel and overlaid on the electrodes. It is noteworthy that reversing the electric field direction does not revert the antipolar phase back into the polar phase, thus suggesting that either the polar phase has been irreversibly converted into the antipolar phase or that conversion of the antipolar phase back to the polar phase requires an electric field along a different direction. Indeed, by applying an electric field along the $[100]_{pc}$ (Fig. 4c), the antipolar phase fully reverts back into the polar phase with near uniformity and is nonvolatile (> 10^6 sec, Extended Data Fig. S18). Finally, reapplication of a lateral electric field along the $[010]_{pc}$ reforms a near-uniform antipolar state between the electrodes by driving the polar/antipolar phase boundary back in a nonvolatile fashion (Fig. 4d), highlighting the complete reversibility of the process. This intriguing behavior that cannot easily be explained by the traditionally-used order parameter – energy diagrams shown in Extended Data S1a,b, but instead, the energy landscape is highly dependent on the initial state of the system (Extended Data S1c-e). We note that while coexistence of antipolar and polar phases and electric field conversion from antipolar to polar states has been reported[53–55], these field-induced phase transitions are typically a volatile saturation of antipolar dipoles along the electric field direction[56,57], relax after relatively short transients, and are not a fundamental change of the ground state of the system. Here, anisotropic electric fields change the energy landscape of the system. The nonvolatile interconversion between the two phases occurs via a nucleation and growth process, which is illustrated in a sequence of SHG images with finer scale electric field steps (Extended Data Fig. S16, S18, S19, and Supplemental Text 7), that depicts the motion of the phase boundary and the non-volatility of the symmetry transformation and confirms the first-order nature of the phase transformation. The nonvolatile transformation between the phases is also confirmed with correlative SHG, PFM, and MIM imaging (Extended Data Figs. 10, 11, and 17 and Supplemental Text 6, 7, and 8) on separate devices, which also demonstrates repeatability.

These electric field-dependent switching processes are sensitive to the orientation of the electric field with respect to the antipolar phase versus the polar phase. In other words, an electric field applied parallel to the polarization wave direction (i.e., $[100]_{pc}$) results in stabilization of the non-centrosymmetric polar phase, while an electric field applied perpendicular to this favors the centrosymmetric antipolar phase, rather than a reorientation of the polarization in the wave. Fig. 1a plots the DFT-computed energies for these three scenarios (in red and green for the polarization waves and orange for the antipolar phase). While the relative energy difference between the two polar phases – those with perpendicularly-oriented polarization waves – is small and nearly the same as the energy of the antipolar phase, the energy barrier between the polar phases in the two orientations is twice as large as that between the polar phase and the antipolar phase (Fig. 4e), due to the similar octahedral tilt patterns of these two phases (top, Fig 4e). As a result, the centrosymmetric antipolar phase is favored over the non-centrosymmetric polar phase under a perpendicularly-applied electric field. We note that there are two kinds of anisotropy imposed on the system: 1) anisotropy in the octahedral tilts arising from the interweaving TSO layer, and 2) the anisotropy arising from the epitaxial strain of the orthorhombic scandate substrates (TSO and GSO). The former strongly affects the switching pathway between polar and antipolar phases, while the latter affects the mesoscale domain formation and length scales of each phase.

Based on the field-dependent imaging of the SHG signal, we record the hysteretic behavior of the SHG intensity as a function of the applied electric field at any given point in the test structure (Fig. 4f; from the location circled in Fig. 4a), where the positive horizontal axis indicates electric field along the $[010]_{pc}$, and the negative horizontal axis denotes electric field along the $[100]_{pc}$. The SHG intensity is manipulated by as much as three orders of magnitude with full non-volatility (stable $>10^6$ sec., Extended Data Fig. S18). We note that, while prior efforts have been dedicated to manipulating the inversion symmetry of materials probed with electric field- and current-driven SHG[28,58–62], as well as geometric patterning[63,64], these effects were typically weaker than those observed here and generally arise from manipulation of electronic band structures, in contrast to overtly manipulating the crystal symmetry

through a phase transition, as is shown here. The field-dependent hysteresis in the SHG data is corroborated by the corresponding hysteretic DC transport (Fig. 4g, also see Extended Data Fig. S22), where the DC resistivity between the two metal electrodes is modulated by over four orders of magnitude; consistent with the range of conductivity observed in each phase in the MIM measurements (Fig. 3), and also consistent with an effective bandgap change of ~0.3 eV. The difference in the coercivity between the SHG (Fig. 4f) and resistivity hysteresis (Fig. 4g) is directly attributed to the fact that the SHG is measured at a single point, whereas the resistivity is a macroscopic manifestation of the connectivity between the metal electrodes.

Outlook

In summary, we have demonstrated a platform by which we can create mixed polar/antipolar phase coexistence in the BFO system by imposing electrostatic and structural boundary conditions upon it. Furthermore, our results show a reversible pathway to convert from one phase to the other with an external electric field, including, remarkably, a mechanism by which an antipolar state can be stabilized with an electric field. Such symmetry and polar order changes are accompanied by dramatic changes in SHG intensity and, more surprisingly, large changes in both the DC and microwave conductivity. It is noteworthy that the significant changes in the SHG and transport behavior, which are a consequence of such a symmetry phase transition, can enable its use as a mechanism in nonvolatile information storage[52], neuromorphic computing[65], and cross-functional devices which take advantage of optical, electronic, and ferroic properties of materials.

Methods

Molecular Beam Epitaxy: Superlattices of alternating $TbScO_3$ and $BiFeO_3$ layers are synthesized by reactive oxide molecular-beam epitaxy in a Veeco GEN10 MBE with *in-situ* reflection high-energy electron diffraction (RHEED) and x-ray diffraction (XRD) using distilled ozone as the oxidant species. $(BiFeO_3)_m/(TbScO_3)_n$, where n and m refer to the thickness, in unit cells, of the $BiFeO_3$ and $TbScO_3$, respectively, are grown on $(110)_O$ $TbScO_3$ and $GdScO_3$ substrates, where the subscript o denotes orthorhombic indices; note that for $TbScO_3$ and $GdScO_3$ $(110)_o=(001)_{pc}$. The superlattices are grown at a substrate temperature between 650 °C and 680 °C in a background pressure of 5×10^{-6} Torr (mmHg) of distilled O_3 (estimated to be 80% pure O_3). Substrate temperatures are measured by an optical pyrometer with a measurement wavelength of 980 nm focused on a platinum layer deposited on the backside of the substrate.

Electrode Patterning and Sputter Deposition: The device electrodes are a bilayer of Ta(4 nm)/Pt(40 nm), where the Ta metal is used as an adhesion layer. The metals were deposited using DC magnetron sputtering (AJA International) at a nominal room temperature with an Ar sputter gas pressure of 2 mTorr and a background base pressure of $\sim 3 \times 10^{-8}$ Torr. Deposition rates for each element were calibrated using X-ray reflectivity measurements of the film thickness. All electrode devices were patterned using a mask-less aligner (Heidelberg Instruments) and standard lift-off processes.

Scanning Transmission Electron Microscopy (STEM): The plan-view and cross-sectional STEM samples of the $[(BiFeO_3)_{14}/TbScO_3)_{10}]$ superlattices were prepared using a FEI Helios focused ion beam (FIB) with a final milling step of 2 keV to reduce damage. The initial sample surface was protected from ion-beam damage by depositing carbon and platinum layers prior to milling. HAADF-STEM images were recorded using a Cs-corrected ThermoFisher Scientific Spectra300 operated at 300 kV, with beam semi-convergence angle of 30 mrad and beam current of 15 pA.

Scanning convergent beam electron diffraction (SCBED) for polarization mapping: We performed SCBED experiments using a second-generation electron microscopy pixel array detector (EMPAD-G2[66]). SCBED works by rastering a focused probe in two-dimensional (2D) real space (x,y) and collecting a full 2D CBED pattern (k_x, k_y) at each probe position, resulting in a 4D dataset[67,68]. Experimental data was acquired using a FEI Titan operated at 300 keV with 10 pA beam current, 2.45 mrad semi-convergence angle, having a probe of ~8 Å FWHM (full-width at half-maximum). The CBED patterns were captured by the EMPAD-G2 with exposure time set to 100 μs per frame, for which a 512 × 512 scan can be recorded in under 2 minutes. Due to dynamical diffraction effects, the charge redistribution due to ferroelectric polarization leads to intensity asymmetry in Friedel pairs of Bragg reflections. We employ Kikuchi bands as a more robust means to extract polarity information against crystal mis-tilts, which often occurs in ferroic oxides due to disinclination strain. By matching with dynamical diffraction simulations, we can unambiguously determine the polarization directions in real space[38–40].

Laboratory-based X-ray diffraction: Structural characterization was performed using a Panalytical X'Pert3 MRD 4-circle diffractometer with a Cu source. Two-dimensional reciprocal space maps were measured around the $TbScO_3$ (220) peak.

Ferroelectric Characterization: Study of the superlattice domain structures was carried out using an atomic force microscope (MFP-3D, Asylum Research). Dual AC resonance tracking piezoforce microscopy (PFM) was conducted using a conductive Pt-coated probe tip (MikroMasch HQ:NSC18/PT) to image the ferroelectric domain structures using lateral and out-of-plane imaging modes. In-plane hysteresis loops were taken using a Radiant Technologies Precision Multiferroic Tester with a frequency of 100 Hz, and an applied voltage of 150 V on patterned interdigitated electrodes (See Fig. S15). The lateral resistivity (ρ) is estimated from the two-point resistance (R) measurement shown in Extended Data

Fig. S22 via ρ=R*L/A, where L=6 μm is the distance between two electrodes and A is the cross-sectional area of the sample where the electric field is applied. We approximate that the electric field is uniform throughout the thickness of the sample. The resistance is always measured across the electrodes along the $[100]_{pc}$ direction, as shown in the images below and now added to the Extended Data. However, we note that the results are similar if the resistance is measured across the electrodes along the $[010]_{pc}$. In other words, the resistivity is isotropic.

Microwave Impedance Microscopy (MIM): The MIM experiments were carried out on a commercial AFM platform (XE-70, Park AFM). The electrically shielded microwave cantilever probes are commercially available from PrimeNano, Inc[45]. The two output channels of MIM correspond to the real and imaginary parts of the local sample admittance, from which the effective ac conductivity of the sample can be deduced. Numerical simulation of the MIM signals was performed by the FEA software COMSOL4.4. Details of the FEA are included in Fig. S12 and Supplementary Text 4.

Second Harmonic Generation (SHG): SHG measurements were carried out in a normal-incidence, reflection-geometry. A Ti/Sapphire oscillator was used for light excitation with ~100 fs pulses and center wavelength of 900 nm, a 78 MHz repetition rate, and an average power of <1 mW. To arbitrarily control the polarization of the incoming light, we use a Glan-Thompson polarizer and subsequently send the light through a half-waveplate. The polarized light was then sent through a short pass dichroic mirror and focused on the sample using an oil immersion objective lens (OL, NA = 1.4). The back-scattered SHG signal was sent through a short pass filter and detected using a spectrometer (SpectraPro 500i, Princeton Instruments) with a charge-coupled device camera (Peltier-cooled CCD, ProEM+: 1600 eXcelon3, Princeton Instruments). A linear polarizer on the back-end optics was used to select emitted light polarization for detection. Diffraction-limited confocal scanning microscopy was used to create SHG intensity maps. A commercial Thorlabs polarimeter was used at the sample location to confirm the

incoming light polarization incident on the sample, as well as the light polarization entering the detector. All SHG maps shown throughout the manuscript were performed using $[100]_{pc}$-polarized incident light (light polarized along the polarization wave orientation) with no polarizer on the back-end optics. *In-situ* DC electric fields are applied to the sample using a Keithley 6430 SUB-FEMTOAMP SourceMeter via a custom, shielded printed circuit board.

SHG Selection Rules: We are working with light incident along the direction $z \sim [001]_{pc}$ so that only the x and y components of the SHG susceptibility tensor are addressed. For the polar point group m with $x \sim [100]_{pc}$ (i.e. spontaneous polarization along x) this leads to the susceptibilities χ_{yyy}, χ_{yxx}, $\chi_{xxy} = \chi_{xyx}$, χ_{xyy}, $\chi_{yyxy} = \chi_{yxy}$ that are expected to be nonzero and can be probed by our experiment. These susceptibilities were used to fit the SHG polarity data in Fig. 2c and 2d.

First-Principles Calculations: Calculations were performed using DFT[69] with the projector augmented wave (PAW) method[70] as implemented in the Vienna *ab initio* simulation package (VASP 5.4.4)[71]. We used a 12x12x12 k-point Γ-centered mesh to sample the Brillouin zone corresponding to a five-atom unit cell and chose an energy cutoff of 850 eV for the plane-wave basis. The following valence electron configurations were used: $6s^2 6p^3$ for bismuth, $3d^7 4s^1$ for iron, and $2s^2 2p^4$ for oxygen. Note that the inclusion of the $5d^{10}$ electrons in the valence manifold for bismuth and the $3p^6$ for iron were tested for bulk structures and gave similar results. The PBEsol + U functional form of the generalized gradient approximation[72] was used, with a commonly used value of $U_{eff} = 4$ eV for the Fe 3d orbitals[73,74], according to Dudarev's approach[75]. No ionic relaxation was carried out in the supercell in which the DOS were computed. The energy barrier calculations were performed by interpolating the ionic positions and volumes linearly between the starting and ending structures and relaxing the electronic structure at fixed ionic positions.

Phase Field Simulations: In the phase-field method, the local free energy density is expressed as a function of the local polarization P_i (i =1-3), local oxygen octahedral tilt order (OTs) θ_i (i =1-3) and antiferroelectric

order parameter (AFEs) qi (i =1-3). The total free energy of a mesoscale domain structure described by the spatial distribution of polarization, oxygen octahedral tilt and antiferroelectric order is then the volume integration of bulk free energy density, elastic energy density, electrostatic energy density and gradient energy density,

$$F = \int \left[\alpha_{ij} P_i P_j + \alpha_{ijkl} P_i P_j P_k P_l + \alpha_{ijklmn} P_i P_j P_k P_l P_m P_n + \beta_{ij} \theta_i \theta_j + \beta_{ijkl} \theta_i \theta_j \theta_k \theta_l + \gamma_{ij} q_i q_j + \gamma_{ijkl} q_i q_{\cdot} \right.$$

,

where $\square_{ij}$, $\square_{ijkl}$, $\square_{ijklmn}$, $\square_{ij}$, $\square_{ijkl}$, $\square_{ij}$, $\square_{ijkl}$, $\square_{ijklmn}$, $\square_{ijkl}$, $\square_{ijkl}$ and h_{ijkl} are local potential coefficients representing the stiffness with respect to the changes in polarization, oxygen octahedral tilt and antiferroelectric order. $\square_{ijkl}$, $\square_{ijkl}$ and $\square_{ijkl}$ are the gradient energy coefficients of polarization, OTs and AFEs, respectively. $\square_b$ is the isotropic background dielectric constant and $\square_0$ is the dielectric constant of free space. The eigenstrain $\square^0$ + is coupled to polarization, AFEs and OTs through $\square_{ij}^0 = \square_{ijkl}\square_i\square_l + \square_{ijkl}\square_i\square_l + \square_{ijlk}\square_i\square_j$, where $\square_{ijkl}$, $\square_{ijkl}$ and $\square_{ijkl}$ are the coupling coefficients.

The temporal and spatial evolution of polarization, OTs and AFEs are governed by the relaxation equations leading to the minimization of the total free energy of the system. In the simulations, periodic boundary conditions are employed along three dimensions. For the mechanical boundary condition, the in-plane directions are clamped while the out-of-plane direction is assumed to be stress-free. A pseudo-2-D mesh of $300 \times 2 \times N$ is used, where N indicates the film thickness and the grid spacing is 0.4 nm. The value of N ranges from 60 to 345 based on different simulation conditions. Paraelectric insulating layers are simulated with different dielectric constants. All simulations are performed for a temperature of 300 K.

References

1. Dagotto, E. *Nanoscale Phase Separation and Colossal Magnetoresistance*. vol. 136 (Springer Berlin Heidelberg, 2003).
2. Uehara, M., Mori, S., Chen, C. H. & Cheong, S. W. Percolative phase separation underlies colossal magnetoresistance in mixed-valent manganites. *Nature* **399**, 560–563 (1999).
3. Ahart, M. *et al.* Origin of morphotropic phase boundaries in ferroelectrics. *Nature* **451**, 545–548 (2008).
4. Yin, Z.-W., Luo, H.-S., Wang, P.-C. & Xu, G.-S. Growth, characterization and properties of relaxor ferroelectric PMN-PT single crystals. *Ferroelectrics* **229**, 207–216 (1999).
5. Robert E Newham. *Properties of Materials: Anisotropy, Symmetry, Structure*. (Oxford University Press, 2004). doi:10.1093/oso/9780198520757.001.0001.
6. Rashba, E. & Sheka, V. Symmetry of Energy Bands in Crystals of Wurtzite Type II. Symmetry of Bands with Spin-Orbit Interaction Included. *Fiz. Tverd. Tela Collect. Pap.* **2**, 62–76 (1959).
7. Lines, M. E. & Glass, A. M. *Principles and applications of ferroelectrics and related materials*. (Oxfrod University Press, 1977).
8. Dzyaloshinsky, I. & I. A thermodynamic theory of "weak" ferromagnetism of antiferromagnetics. *J. Phys. Chem. Solids* **4**, 241–255 (1958).
9. Moriya, T. Anisotropic Superexchange Interaction and Weak Ferromagnetism. *Phys. Rev.* **120**, 91–98 (1960).
10. Goodenough, J. B. The two components of the crystallographic transition in VO_2. *J. Solid State Chem.* **3**, 490–500 (1971).

11. Li, X. *et al.* Terahertz field–induced ferroelectricity in quantum paraelectric $SrTiO_3$. *Science* **364**, 1079–1082 (2019).

12. Nova, T. F., Disa, A. S., Fechner, M. & Cavalleri, A. Metastable ferroelectricity in optically strained SrTiO3. *Science* **364**, 1075–1079 (2019).

13. Lines, M. E. & Glass, A. M. *Principles and Applications of Ferroelectrics and Related Materials*. (Oxford University Press, 2001). doi:10.1093/acprof:oso/9780198507789.001.0001.

14. Das, S. *et al.* Observation of room-temperature polar skyrmions. *Nature* **568**, 368–372 (2019).

15. Yadav, A. K. *et al.* Observation of polar vortices in oxide superlattices. *Nature* **530**, 198–201 (2016).

16. Jia, C. L., Urban, K. W., Alexe, M., Hesse, D. & Vrejoiu, I. Direct observation of continuous electric dipole rotation in flux-closure domains in ferroelectric $Pb(Zr, Ti)O_3$. *Science* **331**, 1420–1423 (2011).

17. Tang, Y. L. *et al.* Observation of a periodic array of flux-closure quadrants in strained ferroelectric $PbTiO_3$ films. *Science* **348**, 547–551 (2015).

18. Ng, S.-W., Noor, N. & Zheng, Z. Graphene-based two-dimensional Janus materials. *NPG Asia Mater. 2018 104* **10**, 217–237 (2018).

19. Mundy, J. A. *et al.* Atomically engineered ferroic layers yield a room-temperature magnetoelectric multiferroic. *Nature* **537**, 523–527 (2016).

20. Bousquet, E. *et al.* Improper ferroelectricity in perovskite oxide artificial superlattices. *Nat. 2008 4527188* **452**, 732–736 (2008).

21. Sichuga, D., Ren, W., Prosandeev, S. & Bellaiche, L. Chiral Patterns of Tilting of Oxygen Octahedra in Zero-Dimensional Ferroelectrics and Multiferroics: A First Principle-Based Study. *Phys. Rev. Lett.* **104**, 207603 (2010).

22. Zhao, H. J., Íñiguez, J., Ren, W., Chen, X. M. & Bellaiche, L. Atomistic theory of hybrid improper

ferroelectricity in perovskites. *Phys. Rev. B* **89**, 174101 (2014).

23. Prosandeev, S., Wang, D., Ren, W., Íñiguez, J. & Bellaiche, L. Novel Nanoscale Twinned Phases in Perovskite Oxides. *Adv. Funct. Mater.* **23**, 234–240 (2013).

24. Diéguez, O., Aguado-Puente, P., Junquera, J. & Íñiguez, J. Domain walls in a perovskite oxide with two primary structural order parameters: First-principles study of $BiFeO_3$. *Phys. Rev. B - Condens. Matter Mater. Phys.* **87**, 024102 (2013).

25. Mundy, J. A. *et al.* Liberating a hidden antiferroelectric phase with interfacial electrostatic engineering. *Sci. Adv.* **8**, 5860 (2022).

26. Dong, W. *et al.* Emergent Antipolar Phase in $BiFeO_3$-$La_{0.7}Sr_{0.3}MnO_3$Superlattice. *Nano Lett.* **20**, 6045 (2020).

27. Cherifi, R. O. *et al.* Electric-field control of magnetic order above room temperature. *Nat. Mater.* **13**, 345–351 (2014).

28. Seyler, K. L. *et al.* Electrical control of second-harmonic generation in a WSe_2 monolayer transistor. *Nat. Nanotechnol.* **10**, 407–411 (2015).

29. Paillard, C., Torun, E., Wirtz, L., Íñiguez, J. & Bellaiche, L. Photoinduced Phase Transitions in Ferroelectrics. *Phys. Rev. Lett.* **123**, 087601 (2019).

30. Pouget, J. P., Launois, H., D'Haenens, J. P., Merenda, P. & Rice, T. M. Electron Localization Induced by Uniaxial Stress in Pure VO_2. *Phys. Rev. Lett.* **35**, 873 (1975).

31. Xu, R. *et al.* Strain-induced room-temperature ferroelectricity in $SrTiO_3$ membranes. *Nat. Commun.* **11**, 3141 (2020).

32. Grosso, B. F. & Spaldin, N. A. Prediction of low-energy phases of $BiFeO_3$ with large unit cells and complex tilts beyond Glazer notation. *Phys. Rev. Mater.* **5**, 054403 (2021).

33. Rispens, G. *et al.* Phase diagram of $BiFeO_3$/ $LaFeO_3$ superlattices studied by x-ray diffraction experiments and first-principles calculations. *Phys. Rev. B - Condens. Matter Mater. Phys.* **90**,

104106 (2014).

34. Carcan, B. *et al.* Phase Diagram of $BiFeO_3$/$LaFeO_3$ Superlattices: Antiferroelectric-Like State Stability Arising from Strain Effects and Symmetry Mismatch at Heterointerfaces. *Adv. Mater. Interfaces* **4**, 1601036 (2017).

35. Diéguez, O., González-Vázquez, O. E., Wojdeł, J. C. & Íñiguez, J. First-principles predictions of low-energy phases of multiferroic $BiFeO_3$. *Phys. Rev. B - Condens. Matter Mater. Phys.* **83**, 094105 (2011).

36. Tate, M. W. *et al.* High Dynamic Range Pixel Array Detector for Scanning Transmission Electron Microscopy. *Microsc. Microanal.* **22**, 237–249 (2016).

37. Zuo, J.-M. & Shao, Y.-T. Scanning Convergent Beam Electron Diffraction (CBED), the Essential Questions of Why, What and How? *Microsc. Microanal.* **24**, 172–173 (2018).

38. Shao, Y.-T. & Zuo, J.-M. Lattice-Rotation Vortex at the Charged Monoclinic Domain Boundary in a Relaxor Ferroelectric Crystal. *Phys. Rev. Lett.* **118**, 157601 (2017).

39. Tsuda, K., Yasuhara, A. & Tanaka, M. Two-dimensional mapping of polarizations of rhombohedral nanostructures in the tetragonal phase of $BaTiO_3$ by the combined use of the scanning transmission electron microscopy and convergent-beam electron diffraction methods. *Appl. Phys. Lett.* **103**, 082908 (2013).

40. Müller-Caspary, K. *et al.* Electrical Polarization in AlN/GaN Nanodisks Measured by Momentum-Resolved 4D Scanning Transmission Electron Microscopy. *Phys. Rev. Lett.* **122**, 106102 (2019).

41. Porter, D. & Easterling, K. E. *Phase transformations in metals and alloys*. (Chapman & Hall, 1992).

42. Damodaran, A. R. *et al.* Phase coexistence and electric-field control of toroidal order in oxide superlattices. *Nat. Mater.* **16**, 1003–1009 (2017).

43. Luca, G. De *et al.* Domain Wall Architecture in Tetragonal Ferroelectric Thin Films. *Adv. Mater.*

29, 1605145 (2017).

44. Chu, Z., Zheng, L. & Lai, K. Microwave Microscopy and Its Applications. *Annu. Rev. Mater. Res.* **50**, 105–130 (2020).

45. Yang, Y. *et al.* Batch-fabricated cantilever probes with electrical shielding for nanoscale dielectric and conductivity imaging. *J. Micromechanics Microengineering* **22**, 115040 (2012).

46. Lai, K., Kundhikanjana, W., Kelly, M. & Shen, Z. X. Modeling and characterization of a cantilever-based near-field scanning microwave impedance microscope. *Rev. Sci. Instrum.* **79**, 063703 (2008).

47. Ahmed, S., Barik, S. K. & Hajra, S. Investigation of electric, dielectric, and magnetic properties of Li^{+1} and Mo^{+6} co-doped $BiFeO_3$. *Appl. Phys. A 2019 1255* **125**, 1–5 (2019).

48. Lu, J. *et al.* Magnetic susceptibility, phonons and dielectric constant of single crystalline $BiFeO_3$. *J. Phys. Conf. Ser.* **200**, 012106 (2010).

49. Lim, J. S. *et al.* Ultrafast collective oxygen-vacancy flow in Ca-doped $BiFeO_3$. *NPG Asia Mater.* **10**, 943–955 (2018).

50. Seidel, J. *et al.* Conduction at domain walls in oxide multiferroics. *Nat. Mater. 2009 83* **8**, 229–234 (2009).

51. Meier, D. *et al.* Anisotropic conductance at improper ferroelectric domain walls. *Nat. Mater. 2012 114* **11**, 284–288 (2012).

52. Edwards, D. *et al.* Giant resistive switching in mixed phase $BiFeO_3$ via phase population control. *Nanoscale* **10**, 17629–17637 (2018).

53. Dawber, M. *et al.* Unusual behavior of the ferroelectric polarization in PbTiO3/SrTiO3 superlattices. *Phys. Rev. Lett.* **95**, 177601 (2005).

54. Shirane, G., Sawaguchi, E. & Takagi, Y. Dielectric Properties of Lead Zirconate. *Phys. Rev.* **84**, 476 (1951).

55. Cross, L. E. Antiferroelectric-Ferroelectric Switching in a Simple “Kittel” Antiferroelectric. *http://dx.doi.org/10.1143/JPSJ.23.77* **23**, 77–82 (2013).

56. Fthenakis, Z. G. & Ponomareva, I. Intrinsic dynamics of the electric-field-induced phase switching in antiferroelectric $PbZrO_3$ ultrathin films. *Phys. Rev. B* **98**, 054107 (2018).

57. Vales-Castro, P. *et al.* Direct Visualization of Anti-Ferroelectric Switching Dynamics via Electrocaloric Imaging. *Adv. Electron. Mater.* **7**, 2100380 (2021).

58. Terhune, R. W., Maker, P. D. & Savage, C. M. Optical Harmonic Generation in Calcite. *Phys. Rev. Lett.* **8**, 404 (1962).

59. Cai, W., Vasudev, A. P. & Brongersma, M. L. Electrically Controlled Nonlinear Generation of Light with Plasmonics. *Science* **333**, 1720–1723 (2011).

60. Kang, L. *et al.* Electrifying photonic metamaterials for tunable nonlinear optics. *Nat. Commun.* **5**, 5680 (2014).

61. Ruzicka, B. A. *et al.* Second-Harmonic Generation Induced by Electric Currents in GaAs. *Phys. Rev. Lett.* **108**, 077403 (2012).

62. Sirtori, C., Capasso, F., Sivco, D. L., Hutchinson, A. L. & Cho, A. Y. Resonant Stark tuning of second-order susceptibility in coupled quantum wells. *Appl. Phys. Lett.* **60**, 151 (1998).

63. Nordlander, J., Rossell, M. D., Campanini, M., Fiebig, M. & Trassin, M. Inversion-Symmetry Engineering in Layered Oxide Thin Films. *Nano Lett.* **21**, 2780–2785 (2021).

64. Canfield, B. K. *et al.* A macroscopic formalism to describe the second-order nonlinear optical response ofnanostructures. *J. Opt. A Pure Appl. Opt.* **8**, S278 (2006).

65. Boyn, S. *et al.* Learning through ferroelectric domain dynamics in solid-state synapses. *Nat. Commun.* **8**, 14736 (2017).

66. Philipp, H. T. *et al.* Very-High Dynamic Range, 10,000 Frames/Second Pixel Array Detector for Electron Microscopy. *Microsc. Microanal.* **28**, 425–440 (2022).

67. Zuo, J. M. & Spence, J. C. H. *Advanced transmission electron microscopy: Imaging and diffraction in nanoscience*. *Advanced Transmission Electron Microscopy: Imaging and Diffraction in Nanoscience* (Springer New York, 2016). doi:10.1007/978-1-4939-6607-3.

68. Ophus, C. Four-Dimensional Scanning Transmission Electron Microscopy (4D-STEM): From Scanning Nanodiffraction to Ptychography and Beyond. *Microsc. Microanal.* **25**, 563–582 (2019).

69. Kohn, W. & Sham, L. J. Self-Consistent Equations Including Exchange and Correlation Effects. *Phys. Rev.* **140**, A1133 (1965).

70. Blöchl, P. E. Projector augmented-wave method. *Phys. Rev. B* **50**, 17953 (1994).

71. Kresse, G. & Furthmüller, J. Efficient iterative schemes for ab initio total-energy calculations using a plane-wave basis set. *Phys. Rev. B* **54**, 11169 (1996).

72. Perdew, J. P., Burke, K. & Ernzerhof, M. Generalized Gradient Approximation Made Simple. *Phys. Rev. Lett.* **77**, 3865 (1996).

73. Neaton, J. B., Ederer, C., Waghmare, U. V., Spaldin, N. A. & Rabe, K. M. First-principles study of spontaneous polarization in multiferroic $BiFeO_3$. *Phys. Rev. B - Condens. Matter Mater. Phys.* **71**, 014113 (2005).

74. Shenton, J. K., Bowler, D. R. & Cheah, W. L. Effects of the Hubbard U on density functional-based predictions of BiFeO3 properties. *J. Phys. Condens. Matter* **29**, 445501 (2017).

75. Dudarev, S. L., Botton, G. A., Savrasov, S. Y., Humphreys, C. J. & Sutton, A. P. Electron-energy-loss spectra and the structural stability of nickel oxide: An LSDA U study. *Phys. Rev. B* **57**, 1505 (1998).

Acknowledgements

R.R., L.W.M., D.A.M., and D.G.S. acknowledge support from the Army Research Office under the ETHOS MURI via cooperative agreement W911NF-21-2-0162. The MIM work (J.Y., D.L., and K.L.) was supported by the Office of Science, Office of Basic Energy Sciences, of the U.S. Department of

Energy under Contract No. DE-SC0019025. Computational resources were provided by ETH Zürich and the Swiss National Supercomputing Center (CSCS), Project ID No. s889. Work at ETH was supported by ETH Zürich and the Körber Foundation. Work at the Molecular Foundry was supported by the Office of Science, Office of Basic Energy Sciences, of the U.S. Department of Energy under Contract No. DE-AC02-05CH11231. L.C. acknowledges financial support from the Ford Foundation and the University of California President's Postdoctoral Fellowship Program. YT.S. and D.A.M acknowledge financial support from the Department of Defense, Air Force Office of Scientific Research under award FA9550-18-1-0480. The electron microscopy studies were performed at the Cornell Center for Materials Research, a National Science Foundation (NSF) Materials Research Science and Engineering Centers program (DMR-1719875). The microscopy work at Cornell was supported by the NSF PARADIM NSF-MRI-1429155, with additional support from Cornell University, the Weill Institute and the Kavli Institute at Cornell. The authors acknowledge fruitful discussions regarding diffraction imaging with Prof. Jian-Min Zuo as well as M. Thomas, J. G. Grazul, M. Silvestry Ramos, K. Spoth for technical support and careful maintenance of the instruments. The authors thank Xiaoxi Huang and Abel Fernandez for fruitful conversations and Prof. Megan E. Holtz for preliminary electron microscopy studies. The authors also acknowledge Isabelle Schulze-Jonack and Markus S. Stypa for help with substrate crystal growth.

Author Contributions

R.R., D.G.S., L.C., and A.B.M. conceived the project and planned the experiments; Y.T.S., and H.K.P. performed transmission electron microscopy (TEM), TEM sample preparation, and atomically-resolved polar and structural analysis under supervision of D.A.M.; A.B.M. optimized synthesis of the superlattices and performed reciprocal space maps under supervision of D.G.S; L.C. and P.B. performed in-situ SHG measurements with help from A.R. and E.B, and M.F.; L.C., P.B, and E.B. prepared the experimental SHG setup; P.B. performed PFM imaging under supervision from L.C.; L.C. and P.B. performed electronic transport measurements. J.Y. and D.L. performed microwave impedance microscopy and analysis with supervision from K.L. M.M. performed lab-based x-ray structural

characterization and analysis; L.C. and E.P designed and microfabricated the electric field devices. L.C. deposited metal layers; First-principles calculations were performed by B.F.G. under supervision of N.S.; Phase field calculations were performed by C.D. and F.X. under the supervision of L.-Q. C. and X.G. under the supervision of Z.H.; SHG analysis was completed by L.C., P.B, and M.F.; Scandate crystal substrates were grown by S.G.; L.C., Y.T.S., R.R, K.L., and L.W.M. wrote the manuscript.

Conflict of Interest

K.L. holds a patent on the MIM technology, which is licensed to PrimeNano, Inc., for commercial instruments. The terms of this arrangement have been reviewed and approved by the University of Texas at Austin in accordance with its policy on objectivity in research. The remaining authors declare no conflict of interest.

Additional Information

Correspondence and request for materials should be addressed to R.R. and L.C.

Data Availability

The data supporting the findings of this study are available within the paper and other findings of this study are available from the corresponding authors upon reasonable request.

Figures

Figure 1

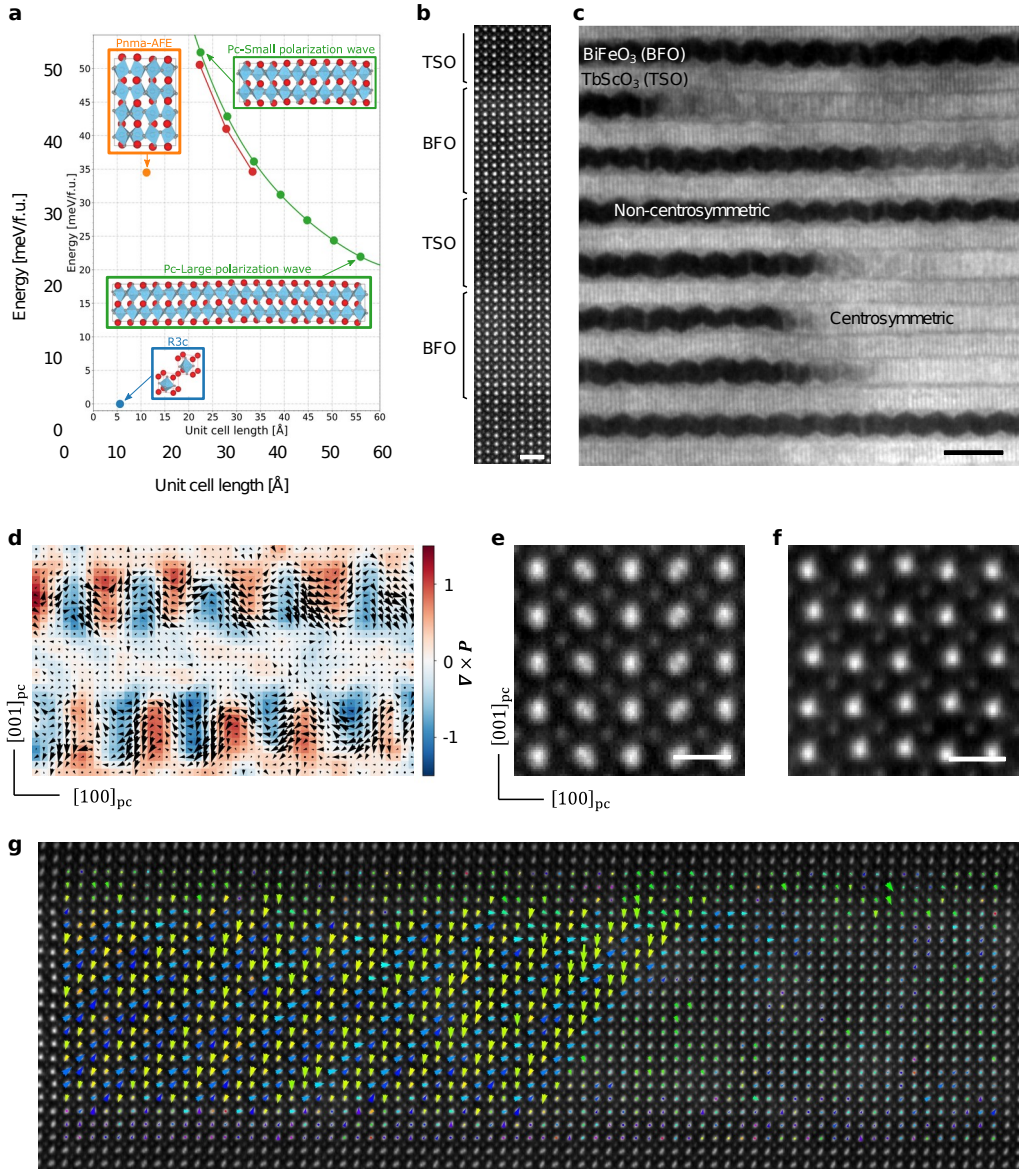

Figure 1 | Mixed-phase coexistence of polar and antipolar phases in the BFO/TSO superlattice. a) Structures, energies, and lattice constants of low-energy phases of BFO with zero out-of-plane net polarization predicted using DFT. **b)** Atomically-resolved HAADF-STEM image of the $[(BFO)_{14}/(TSO)_{10}]_{20}$ superlattice along the $[010]_{pc}$ zone axis showing atomically sharp interfaces. Scale bar is 10 nm. **c)** Bright-field image obtained from the SCBED dataset showing the spatial distribution of polar (*Pc*) and anti-polar (*Pnma*) BFO phases. Scale bar is 10 nm. **d)** Polarization map of the polar phase overlaid with its curl ($\nabla \times \vec{P}$) obtained by analyzing the Kikuchi bands recorded in the SCBED dataset using an EMPAD. Scale bar is 5 nm. Atomic resolution HAADF-STEM images of the **e)** anti-polar phase along $[010]_{pc}$ (left)

and **f)** $[100]_{pc}$ (right) zone axes. Scale bar is 5 Å. **g)** HAADF-STEM image along $[100]_{pc}$ showing the atomically sharp interface between the antipolar and polar phases. The vectors represent the displacement of Bi atomic columns relative to the four neighboring Fe columns, showing the "up-up/down-down" distortion along the 45º in the antipolar region. Scale bar is 2 nm.

Figure 2

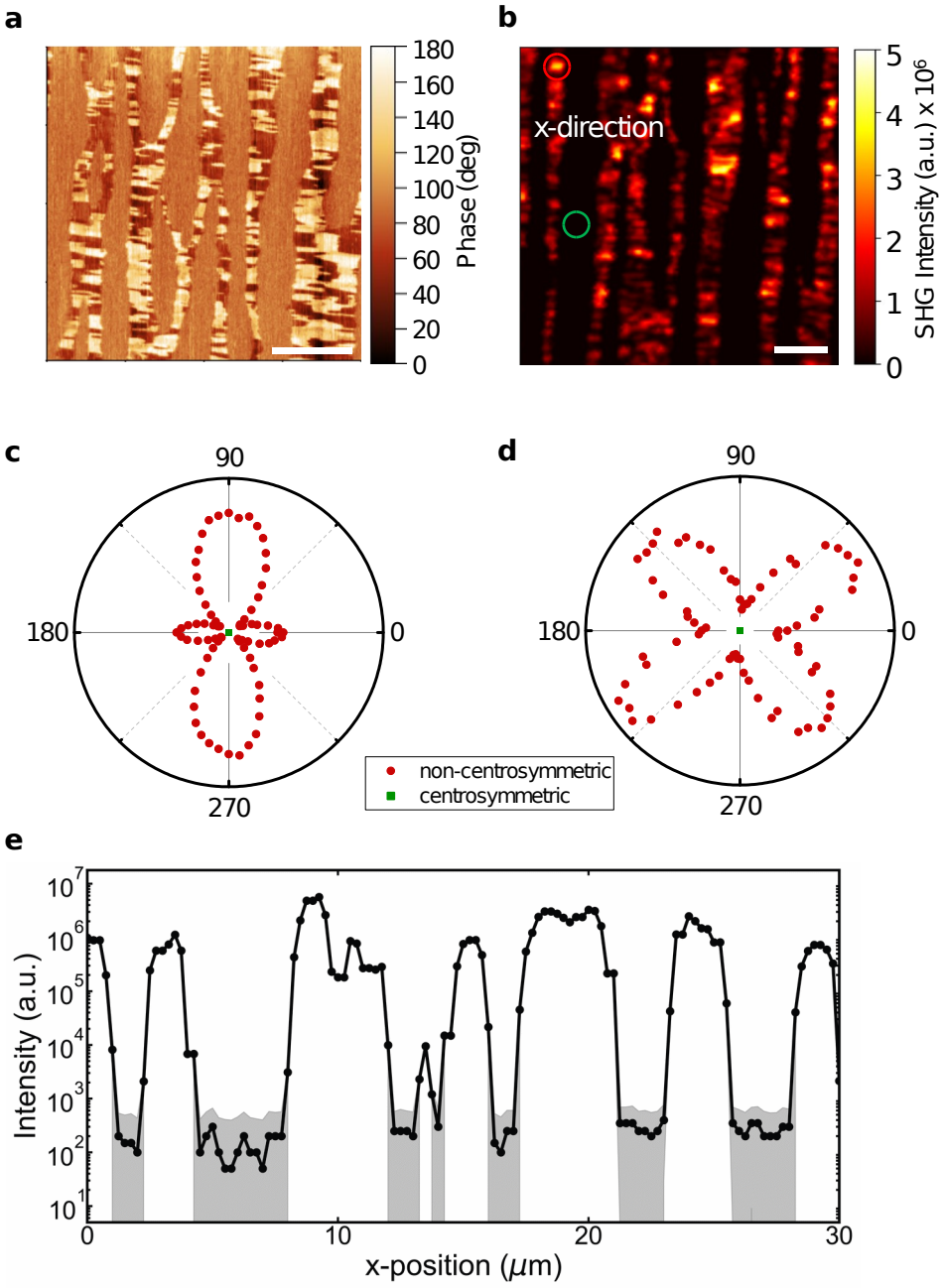

Figure 2 | Piezoforce and nonlinear optical response of mixed-phase coexistence. a) PFM phase image of the $[(BFO)_{14}/(TSO)_{10}]_{20}$ superlattice. Dark regions with near 0° phase angle denote net polarization along the $[100]_{pc}$ direction, as indicated by the white arrow, whereas light regions with near 180° phase denote net polarization along the $[\bar{1}00]_{pc}$ direction, as indicated by the black arrow. Areas exhibiting 90° phase have no net polar order and reflect antipolar regions. **b)** Confocal SHG map on a nearby area of the same sample. Areas showing high (low) SHG intensity contain (non-)centrosymmetric BFO. Local SHG polar plots from the red and green circled regions in (b) are shown in (c) and (d), where the incident light polarization (θ) is varied and the corresponding **c)** vertically or **d)** horizontally polarized emitted light at the second harmonic is analyzed. Red and green regions correspond to non-centrosymmetric and centrosymmetric phases, respectively. **e)** SHG intensity line profile along the dashed white line in (b). The uncertainty (grey bands) come from the noise level of the SHG detector. Scale bars are 5 μm. a.u., arbitrary units.

Figure 3

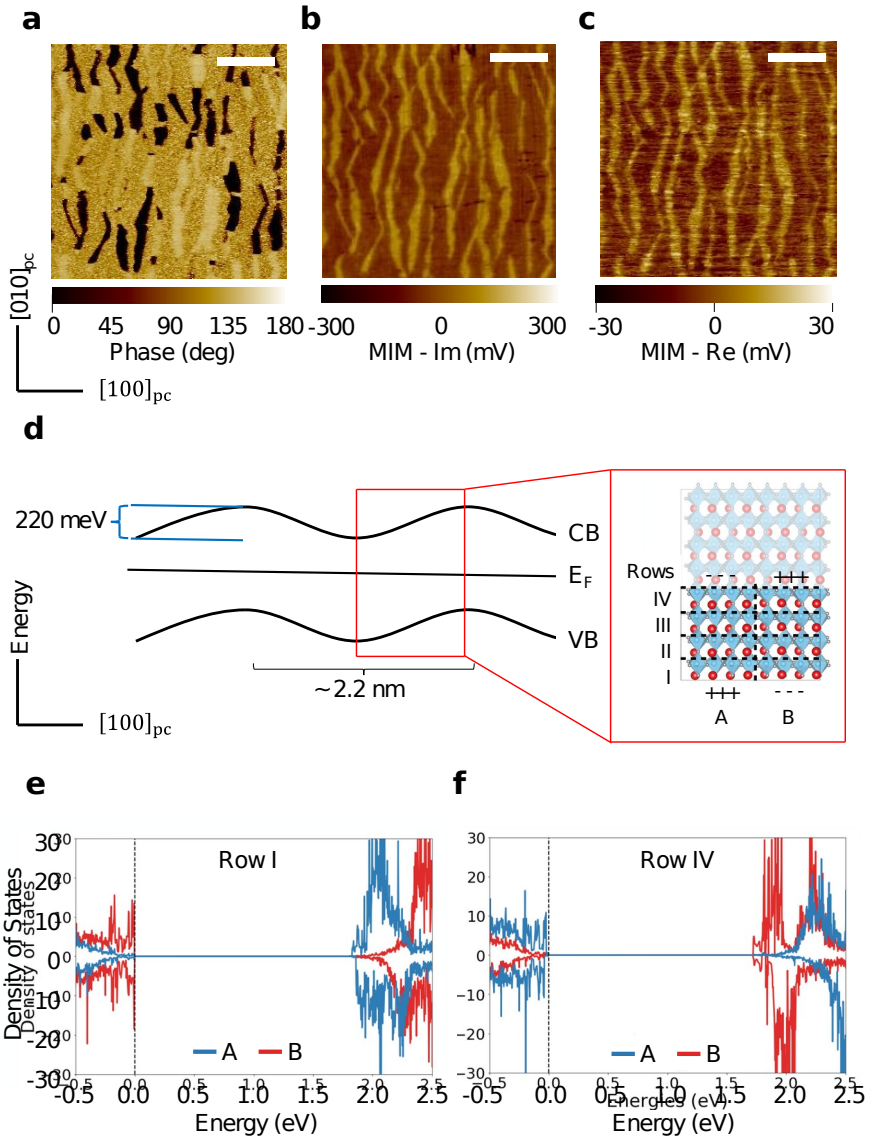

Figure 3 | Microwave impedance microscopy (MIM) and DFT band structure calculations. a) PFM phase image of a TSO//$[(BFO)_{14}/(TSO)_{10}]_{20}$ superlattice, where the contrast is sensitive to polarization along the $[100]_{pc}$ direction. **b)** Imaginary (Im) and **c)** real (Re) parts of the MIM images taken at the same area as (a). Scale bars in (a-c) are 2 μm. **d)** Band bending model of the conduction and valence bands, reducing the effective bandgap of the system by ~0.45 eV. Red "zoomed-in" box shows a labeled real-space schematic of the modeled polarization wave. **e,f)** DFT-computed density of states for a confined polarization wave heterostructure with 2.2 nm periodicity in the two regions indicated in (d), where a built-in voltage is established by $[001]_{pc}$-oriented component of the wave polarization.

5

Figure 4

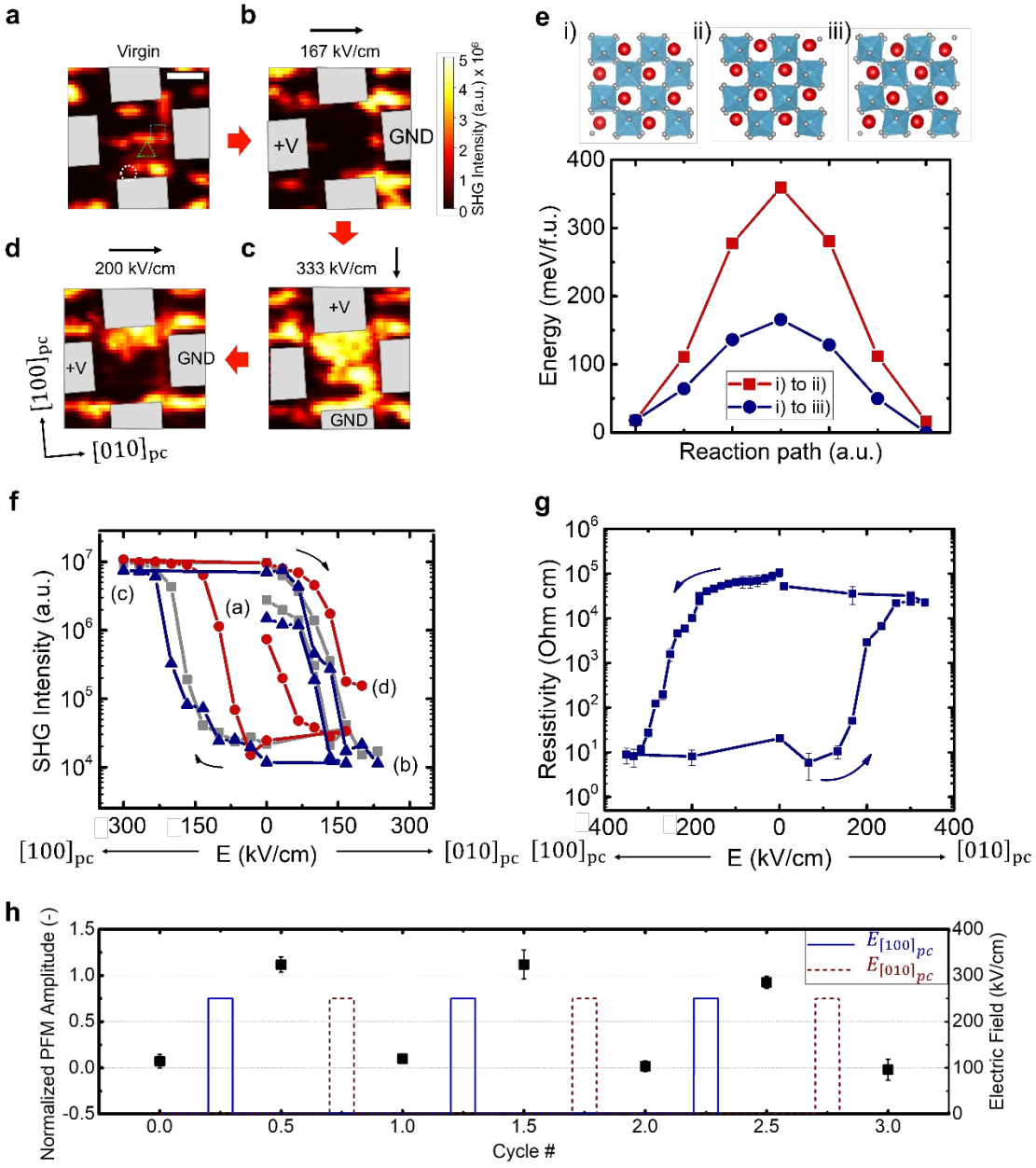

Figure 4 | Nonvolatile electric field manipulation of SHG intensity and resistivity. a-d) A series of SHG maps under sequentially applied orthogonal in-plane electric fields. Electrodes are denoted by grey overlaid boxes, where the active region of the sample is located between the four electrodes. The magnitude and orientation of the electric field are denoted by the arrows and text above each panel and on each electrode. Red arrows between each panel denote the sequence of applied electric field. Scale bar is 3 μm. **e) (top)** Structures of i), ii) the polar wave phases with perpendicular polarization orientations, as well as iii) the antipolar phase. Note the differences in the tilt patterns between the two polar phases; the tilt pattern of the antipolar phase is a close match to that of the initial polar phase. (bottom) Energy barriers computed by linearly interpolating between the different phases. **f)** An SHG-electric field hysteresis loop for the regions outlines in (a) showing an approximately three orders of magnitude change in SHG intensity. Each plotted symbol type (circle, square, triangle) corresponds to

local hysteresis of the same shape in (a). The positive (negative) horizontal axis denotes electric field oriented along the $[010]_{pc}$ ($[100]_{pc}$) direction. SHG uncertainty corresponds to the background noise of the detector and is smaller than the data points. **g)** Hysteresis of DC resistivity with electric field across the top and bottom electrodes in the device. The positive (negative) horizontal axis denotes electric field oriented along the $[010]_{pc}$ ($[100]_{pc}$) direction. Error bars in the resistivity denote uncertainty of the leakage current during the measurement. **h)** Normalized PFM amplitude of three electric field device cycles, with alternating fields alternative along $[100]_{pc}$ and $[010]_{pc}$ directions between each half cycle as indicated. Error bars are the standard error in PFM amplitude from various points within the device.